

Short pulse generation from a graphene-coupled passively mode-locked terahertz laser

Received: 22 July 2022

Accepted: 8 March 2023

Published online: 20 April 2023

 Check for updates

Elisa Riccardi^{1,7}, Valentino Pistore^{1,7}, Seonggil Kang², Lukas Seitner³, Anna De Vetter², Christian Jirauschek^{3,4}, Juliette Mangeney², Lianhe Li⁵, A. Giles Davies⁵, Edmund H. Linfield⁵, Andrea C. Ferrari⁶, Sukhdeep S. Dhillon² & Miriam S. Vitiello¹✉

The generation of stable trains of ultrashort (femtosecond to picosecond), terahertz-frequency radiation pulses with large instantaneous intensities is an underlying requirement for the investigation of light–matter interactions for metrology and ultrahigh-speed communications. In solid-state electrically pumped lasers, the primary route to generate short pulses is through passive mode-locking; however, this has not yet been achieved in the terahertz range, defining one of the longest standing goals over the past two decades. In fact, the realization of passive mode-locking has long been assumed to be inherently hindered by the fast recovery times associated with the intersubband gain of terahertz lasers. Here we demonstrate a self-starting miniaturized short pulse terahertz laser, exploiting an original device architecture that includes the surface patterning of multilayer-graphene saturable absorbers distributed along the entire cavity of a double-metal semiconductor 2.30–3.55 THz wire laser. Self-starting pulsed emission with 4.0-ps-long pulses is demonstrated in a compact, all-electronic, all-passive and inexpensive configuration.

In laser physics, mode-locking is a fundamental set of techniques that allows for the generation of ultrashort light pulse trains with large instantaneous intensities from a laser source^{1,2}. Owing to their remarkable stability³, high peak-power (up to hundreds of watts)^{4,5}, short duration (100 fs to tens of picoseconds)⁶ and coherent emission over a broad bandwidth⁶, mode-locked laser sources benefit an exceptional variety of applications and research in ultrafast phenomena⁷. Furthermore, frequency combs⁸ can be generated from stabilized mode-locked lasers⁹, and hence are key for quantum metrology, sensing, communication and spectroscopy⁹.

Passive mode-locking techniques—which rely on semiconductor saturable absorber mirrors¹⁰ or nonlinear phase shifts^{11,12}—are commonly used to generate short pulses from the ultraviolet (from $\lambda \approx 200$ nm; ref. 13) to the mid-infrared (up to $\lambda \approx 3.5$ μm ; ref. 14). At longer wavelengths such as terahertz frequencies ($\lambda \approx 30$ – 300 μm), the lack of suitable gain media has resulted in the adoption of different strategies to generate pulsed laser radiation, either through optical rectification processes using femtosecond optical lasers¹⁵—although with limited (approximately microwatt) output power and efficiency ($\eta < 6\%$)¹⁶—or complex, non-tabletop and expensive

¹NEST, CNR—Istituto Nanoscienze and Scuola Normale Superiore, Pisa, Italy. ²Laboratoire de Physique de l'Ecole Normale Supérieure ENS, Université PSL, CNRS, Sorbonne Université, Université de Paris, Paris, France. ³TUM School of Computation, Information and Technology, Technical University of Munich, Garching, Germany. ⁴TUM Center for Quantum Engineering (ZQE), Garching, Germany. ⁵School of Electronic and Electrical Engineering, University of Leeds, Leeds, UK. ⁶Cambridge Graphene Centre, University of Cambridge, Cambridge, UK. ⁷These authors contributed equally to this work: Elisa Riccardi, Valentino Pistore. ✉e-mail: miriam.vitiello@sns.it

set-ups such as free electron lasers¹⁷, hindering their use beyond basic research.

Quantum cascade lasers (QCLs) are the only miniaturized direct sources of laser radiation in the terahertz frequency range, combining chip-scale size, high (>1 W) power emission, high spectral purity and broad bandwidth¹⁸. Although room-temperature operation is yet to be achieved, Fabry–Perot terahertz QCLs can operate in a compact Peltier cooler configuration up to 261 K (ref. 19) and generate trains of short pulses by active mode-locking^{20–22}, that is, by modulating the gain and losses in the active medium with a bias current modulation. Active techniques are favoured by the QCL ultrafast carrier dynamics, inherent to the intersubband transitions in the gain medium²³. The gain in a QCL recovers from its saturated value much faster than the cavity round-trip time (~72 ps for a standard 3-mm-long cavity) and the photon lifetime²⁴, resulting in gain recovery times spanning from ~2 ps (ref. 25) to 34–50 ps (ref. 26). This is the result of very strong electron–electron and electron–phonon interactions in the QCL polar semiconductor gain media, which induce an ultrafast non-radiative intersubband relaxation²⁶. This, in turn, prevents the successful use of conventional passive mode-locking techniques based on lumped absorbers²⁷, as local perturbations of the photon population are quickly reabsorbed by the fast gain that rapidly restores a quasi-continuous-wave emission profile^{28,29}. Recent approaches for short pulse emission in terahertz QCLs are therefore all based on active schemes. These include dispersion compensation of the active region, leading to the generation of a train of 4-ps-long pulses²⁰, or generation of shorter isolated pulses (2.5 ps)²², albeit with a duration limited by the slow electrical modulation employed in the active mode-locking³⁰. The latter, which makes inefficient use of the gain, also requires dedicated external electronics and connections, impacting its widespread adoption.

Pulse trains generated by soliton-like mode-locking were reported in quantum cascade ring lasers^{24,31}. Although they do not require a saturable absorber or external active modulation, they rely on the balancing action of anomalous chromatic dispersion and Kerr non-linearity to generate temporally and spectrally immutable pulses. Soliton formation was predicted and demonstrated in mid-infrared ring QCLs³², but required spectral filtering at the output due to the presence of an additional dispersive wave. This approach cannot be exploited in Fabry–Perot architectures.

The realization of self-starting short pulse emission from terahertz QCLs is highly desirable for a variety of applications and for providing a compact alternative to bulky terahertz time-domain systems³³. Theoretical predictions of design strategies (that is, interleaved gain and absorbing periods with appropriate dipole moments)³⁴ have been followed by the encouraging experimental observation of Rabi-flopping in mid-infrared QCLs³⁵; however, at terahertz frequencies, engineering intracavity semiconductor multilayers with stringent requirements of the gain and absorption faces fundamental obstacles due to the extremely small photon energies involved.

Here we demonstrate passive mode-locking in a semiconductor heterostructure laser operating at terahertz frequencies. By employing a heterogeneous gain medium^{36,37} and an architecture that integrates a distributed graphene saturable absorber (DGSA) on the top-surface of the double-metal QCL cavity, we achieve self-starting pulsed emission with 4.0-ps-long pulses in a compact, all-electronic, all-passive and inexpensive configuration. We take advantage of graphene saturable absorption's high transparency modulation (~80%)³⁸ and fast recovery times (2–3 ps)^{39,40} (faster than the gain recovery time in terahertz QCLs) while the intracavity terahertz radiation experiences saturable losses, which favours pulsed emission over naturally occurring continuous-wave emission.

Detailed electromagnetic simulations of the QCL structure and light–matter interactions in the active medium corroborate our findings, confirming the robustness of our approach. The proposed scheme can be applied to any semiconductor heterostructure laser, including

mid-infrared QCLs, with claims of passive mode-locking of QCLs operating in the mid-infrared⁴¹ reinterpreted as coherent dynamic instabilities resulting from the extremely fast gain recovery time of this family of class-A lasers^{24,25}.

Results

The QCL gain medium comprises nine GaAs quantum wells, which form a cascade of alternating photon and longitudinal-optical-phonon-assisted transitions between two quasi-minibands³⁶. The gain medium consists of a 17- μm -thick GaAs/AlGaAs heterostructure featuring three active regions with gain bandwidths centred at 2.5, 3 and 3.5 THz, and comparable threshold current densities. The double-metal Fabry–Perot laser cavity includes top nickel-based lossy side absorbers to suppress high-order lateral modes (Methods)²². A 2.9-mm-long and 85- μm -wide reference Fabry–Perot QCL was fabricated with a set of 6.5- μm -wide side absorbers (see ref. 37 for transport and optical data), whereas a 2.3-mm-long and 49- μm -wide QCL with 0.5- μm -wide side absorbers was prepared for multilayer graphene (MLG) integration. Two 4- μm -wide stripes—aligned with the waveguide longitudinal axis and centred 12 μm from each edge—were lithographically defined onto the top gold layer, exposing the active region below. The DGSA was realized by transferring a seven-layer chemical-vapour-deposition-grown MLG film on top of the etched stripes (see Fig. 1a–c, Methods, and Supplementary Figs. 1 and 2). The MLG on the gold contact outside of the stripes is removed to allow for the application of the bonding wires (Fig. 1b), whereas the MLG ensures a homogeneous covering of the active region (Fig. 1c).

Multilayer graphene is shaped as a couple of stripes to introduce an additional loss component to the QCL waveguide; however, the intracavity electric field can saturate this loss—opening a net gain window that favours pulse formation. As MLG is distributed continuously along the entire cavity, this effect is not destroyed by the 2–3 ps fast gain recovery time of the investigated terahertz QCL active region, which would happen if MLG was placed at a single point along the QCL cavity. The position of the DGSA stripes (12 μm away from the waveguide centre) is chosen to guarantee at least 50% larger waveguide losses for TM_{01} compared with TM_{00} . Their width (4 μm each) results from a trade-off that ensures a sufficient overlap of the electric field on MLG while avoiding excessive losses with respect to the reference QCL.

The DGSA-QCL was simulated via COMSOL Multiphysics. The MLG is included as a transition boundary condition with refractive index \tilde{n}_g determined by terahertz time-domain spectroscopy (TDS) experiments (Tera K5 by MenloSystems) performed on the nominally same MLG film transferred onto an undoped GaAs substrate, resulting in a complex refractive index $\tilde{n}_g = 16.9 + i49.2$ at 3 THz (Supplementary Fig. 3). The highly doped n^+ layer ($n = 2 \times 10^{18}$) between the active region and the top gold contact is also included in the model. Figure 1d shows the electric field intensity distribution in a cross-section of the QCL cavity at 3 THz; MLG affects the distribution across the interface at the active region/gold top contact/air boundary at $y = 17 \mu\text{m}$, inducing the concentration of the electric field on the MLG. Refs. 38,42 showed that a strong terahertz electric field can saturate the graphene absorption, α_g , which results in a decrease of the imaginary part of its complex refractive index k_g due to its proportionality to the absorption coefficient $\alpha_g = 4\pi k_g/\lambda_0$, where λ_0 is the radiation wavelength.

We then simulated the DGSA-induced waveguide losses spectra for the TM_{00} mode at 3 THz for different values of the imaginary part of the MLG refractive index (Fig. 1e).

The losses for each frequency have a maximum, as marked by the black dashed line on the map. Below this curve, a reduction of $\text{Im}(\tilde{n}_g)$ corresponds to lower losses, that is, the MLG stripes behave as a DGSA. $\text{Im}(\tilde{n}_g)$, as extracted from terahertz TDS, is represented by the purple dashed line in Fig. 1e. This guarantees DGSA operation at least for all frequencies >2.5 THz. The TM_{00} and TM_{01} waveguide losses decrease for stronger saturation, thus leading to a net round-trip gain for pulsed over continuous wave emission. The opposite would be true if $\text{Im}(\tilde{n}_g)$

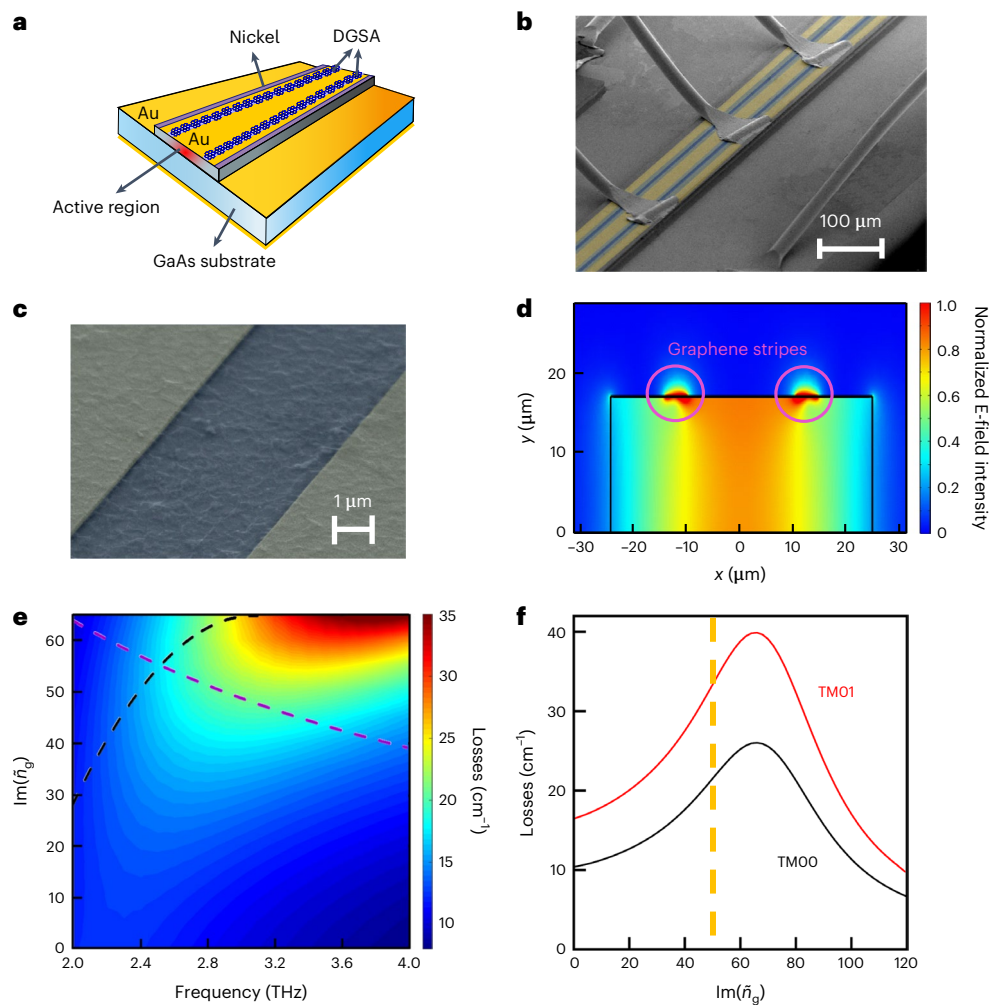


Fig. 1 | Device schematics and optical simulations. **a**, Three-dimensional schematic of the device structure. The DGSA is integrated onto the gold top layer contact of the QCL waveguide. **b**, False-colour scanning electron microscope image of a double-metal QCL with an integrated DGSA. **c**, Magnified image over a portion of the QCL cavity, showing the gold top contact with the 4 μm etched stripes covered by the MLG (in blue). **d**, Simulated electric field intensity distribution in the cross-section of the DGSA-QCL at 3 THz. The violet circles highlight the MLG stripes. The MLG refractive index is set to $\tilde{n} = 16.9 + i49.2$ as measured via terahertz TDS (see Supplementary Fig. 3). **e**, Colour map of

the waveguide loss spectrum for different values of the MLG refractive index imaginary part. The black dashed line is the maximum of the losses for each frequency (the MLG operates as a DGSA when the imaginary part of the refractive index is below this line), whereas the purple dashed line is the imaginary part of the MLG refractive index as extracted from terahertz TDS experiments. **f**, Simulated waveguide losses for TM₀₀ and TM₀₁ modes as a function of the imaginary part for $\text{Re}(\tilde{n}_g) = 16.9$ at 3 THz. For $\text{Im}(\tilde{n}_g) < 65$ (with $\text{Im}(\tilde{n}_g) = 65$ being the loss maximum at 3 THz), a reduction of $\text{Im}(\tilde{n}_g)$, induced by saturable absorption leads to a net round-trip gain, favouring pulse formation.

were above the loss maximum. Figure 1f shows the TM₀₀ and TM₀₁ mode losses at 3 THz as a function of $\text{Im}(\tilde{n}_g)$. The starting $\text{Im}(\tilde{n}_g)$ corresponds to the orange dashed line, so the TM₀₁/TM₀₀ ratio is 55–60% regardless of intracavity field intensity. The saturable and non-saturable absorption coefficients can also both be extracted for the TM₀₀ mode, each having an approximate value of 10.5 cm^{-1} , by comparing the losses at $\text{Im}(\tilde{n}_g) = 49.2$ and $\text{Im}(\tilde{n}_g) = 0$.

Figure 2a shows the continuous wave current density–voltage and light–current density characteristics of the DGSA-QCL. The threshold current density ($J_{\text{threshold}} \approx 170 \text{ A cm}^{-2}$) of the reference QCLs³⁷ proves that the DGSA architecture does not greatly affect $J_{\text{threshold}}$ (180 A cm^{-2}). The QCL delivers a maximum optical power in continuous wave of 8 mW and has a slope efficiency of 46 mW A^{-1} .

The Fourier-transform infrared spectra (FTIR, Bruker, Vertex 80; Fig. 2b,c) above the whole band alignment (Fig. 2b), and in the region of maximum spectral coverage just above the maximum of the optical power (Fig. 2c), show that the QCL bandwidth progressively increases from 0.9 to 1.25 THz. Furthermore, in these regimes, the modes seem phase-locked, as indicated by the sharp ($\sim 38 \text{ dBm}$) and

narrow (1–5 kHz) intermode beatnotes (Fig. 2d,e), which provide a signature of a genuine comb operation. The emission of such a terahertz QCL operating as a frequency comb is generally a mixture of frequency- and amplitude-modulated output²⁴, with a periodicity given by the cavity roundtrip.

The intermode beatnote map, plotted as a function of the driving current (Fig. 2d), shows that the comb regime in the DGSA laser persists at first for almost 100 mA (that is, the bias region of the reference laser³⁷) and then immediately before and across the negative differential resistance (NDR) region. Conversely, the reference structure³⁷ behaves as a fully stabilized comb⁴³ only above the onset of band alignment and for a current range of $\sim 106 \text{ mA}$ (ref. 37), regardless of cavity dimensions^{37,44}. In fact, it is usually difficult to operate a QCL as a frequency combs close to the NDR region, as the high group-velocity dispersion (GVD) occurring in the region of high electric field domains prevents the modes from achieving stable phase-locking⁴⁵. In the current regime in-between (350–570 mA), the linewidth is $> 10^8 \text{ Hz}$, as it is in the reference structure for $J/J_{\text{threshold}} > 1.4$ (refs. 37,44)—a signature of mostly chaotic behaviour of the modal phases.

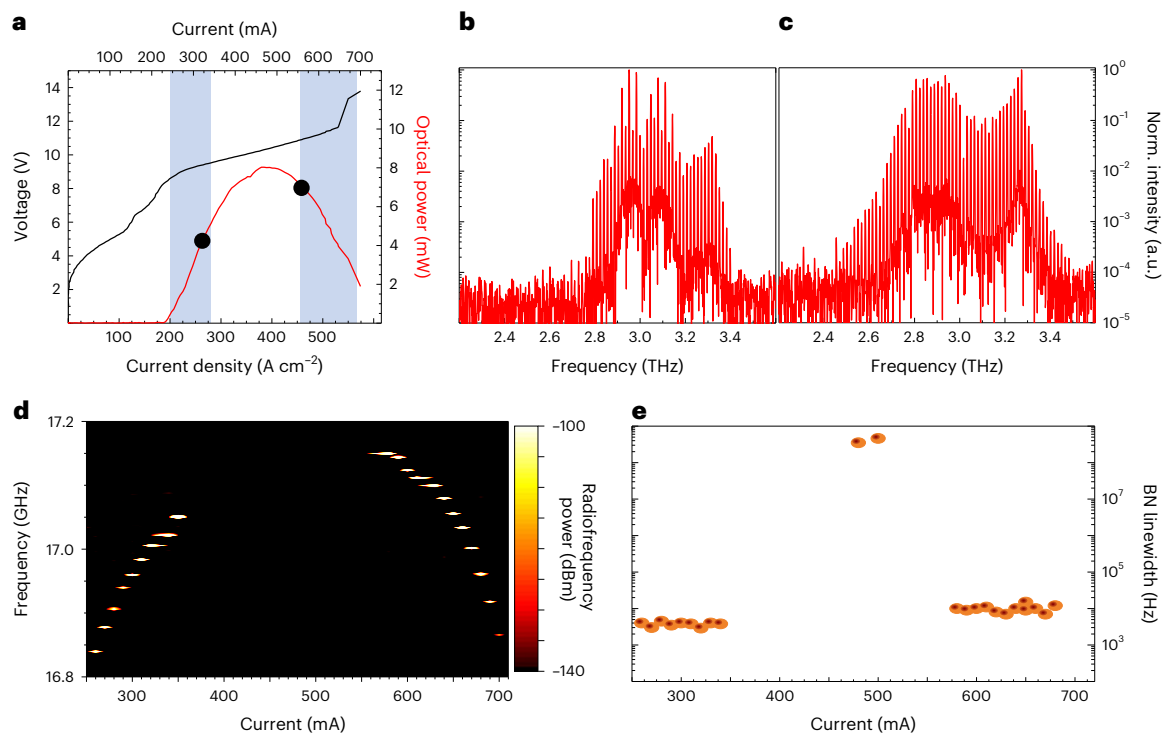


Fig. 2 | Electrical and optical characterization of the DGSA-QCL. a, Voltage–current density and light–current density characteristics measured at 20 K in continuous wave. The two shaded blue areas correspond to the bias ranges in which the device shows a single and narrow intermode beatnote. The optical power was measured using a broad-area terahertz absolute power meter

(TK Instruments, aperture 55 × 40 mm²). **b, c**, FTIR spectra acquired under vacuum at 340 mA (**b**) and 570 mA (**c**) at 20 K with a 0.075 cm⁻¹ spectral resolution. **d**, Intermode beatnote map as a function of DGSA-QCL driving current, measured at 20 K with a 10 mA current step. **e**, Linewidths of the beatnotes in **d**.

The analysis of the beatnote linewidths shows a general agreement with the values extracted on reference lasers (2–8 kHz)^{37,44}, whereas much smaller linewidths (600 Hz) are obtained when GVD compensation schemes are adopted⁴⁴. This means that, as expected, the DGSA architecture does not affect the GVD and suggests that the appearance of a single and narrow beatnote at driving currents >570 mA is indicative of a different physical mechanism to that operated on the QCL by the GSA. Similar results (Supplementary Fig. 4) have been achieved on a second DGSA-QCL with the same active region, 15 graphene layers and different cavity dimensions (3.13 mm × 68 μm × 17 μm), also with substantial reduction of the beatnote linewidth for threshold currents >550 Acm⁻¹.

We next measured the emission profile of the DGSA in the time domain with a coherent technique, gaining access to the amplitude and phase information of the emitted electric field. To this aim, we performed a coherent measurement based on injection seeding⁴⁶, previously used to show pulsed behaviour induced in terahertz QCLs by active mode-locking⁴⁶. Such a technique allows measurement of the free-running QCL emission with a temporal resolution better than 100 fs.

Figure 3a plots a 250-ps-long time-trace of the electric field emitted by the reference QCL (ref. 37) biased at 663 mA ($I/I_{\text{threshold}} = 1.70$), acquired 1 ns after the seeding pulse injection, that is, well into the steady-state regime where no effect of the initial pulse persists. No applied modulation at the QCL round-trip frequency is here present, as it instead occurs in the case of active mode-locking. The quasi continuous-wave profile combined with amplitude modulations on a short time scale (<5 ps) is a typical consequence^{47,48} of the interplay between the QCL fast gain recovery time²⁶ and the giant Kerr non-linearity⁴⁹ arising from Bloch gain⁴⁸. The spectrum (Fig. 3b), obtained by Fourier-transforming the electric field time trace, shows broadband emission from 2.2 to 3.3 THz, in agreement with the FTIR

spectra measured under vacuum^{37,44}. The latter, however, shows modes up to 3.45 THz and an even power distribution between the two bands centred at 2.8 and 3.2 THz, meaning that the higher frequency band is more attenuated in the TDS spectrum than the band at lower frequencies. This is consistent with the presence of the absorption at 3.7 THz of the ZnTe crystal⁵⁰ used for coherent electro-optic sampling.

Figure 3c plots the free-running emission of the DGSA-QCL, biased at 327 mA ($I/I_{\text{threshold}} = 1.68$) in the regime characterized by a 3-kHz-broad beatnote. The electric field profile reveals the generation of a pulsed profile, demonstrating that the QCL can be passively mode-locked by our GSA. The spectrum retrieved by fast-Fourier transforming the electric field (Fig. 3d) matches that measured by the FTIR at the same bias (Fig. 2b), aside from the attenuation at higher frequencies due to the ZnTe crystal absorption profile. Figure 3e is the electric field amplitude profile of one of the pulses emitted by the DGSA-QCL -1 ns after the seeding pulse injection. The corresponding pulse intensity profile in Fig. 3f reveals a -6.1 ps duration, as extracted from the Gaussian fit (red dashed line). When the QCL is driven at 570 mA, where the number of emitted modes becomes much larger (Fig. 2c), the optical power per comb tooth reaches 0.12 mW and, with a sharp and narrow beatnote still present, a pulsed behaviour is once again retrieved (Fig. 3g). As expected, the broader bandwidth gets translated into a shorter pulse duration. This is evident from the intensity profile of the electric field in Fig. 3h, which shows a 4 ps pulse generation.

Figure 3c,e shows small regular pulses in between the cavity round-trips. This could be an indication that the absorption is not fully saturated. At higher currents (570 mA), that is, higher terahertz QCL power, the intensity of these secondary pulsations indeed decreased to nearly zero (Fig. 3g).

We performed time-domain simulations⁵¹ to study the pulse formation mechanism of our DGSA-QCL and shed light on the

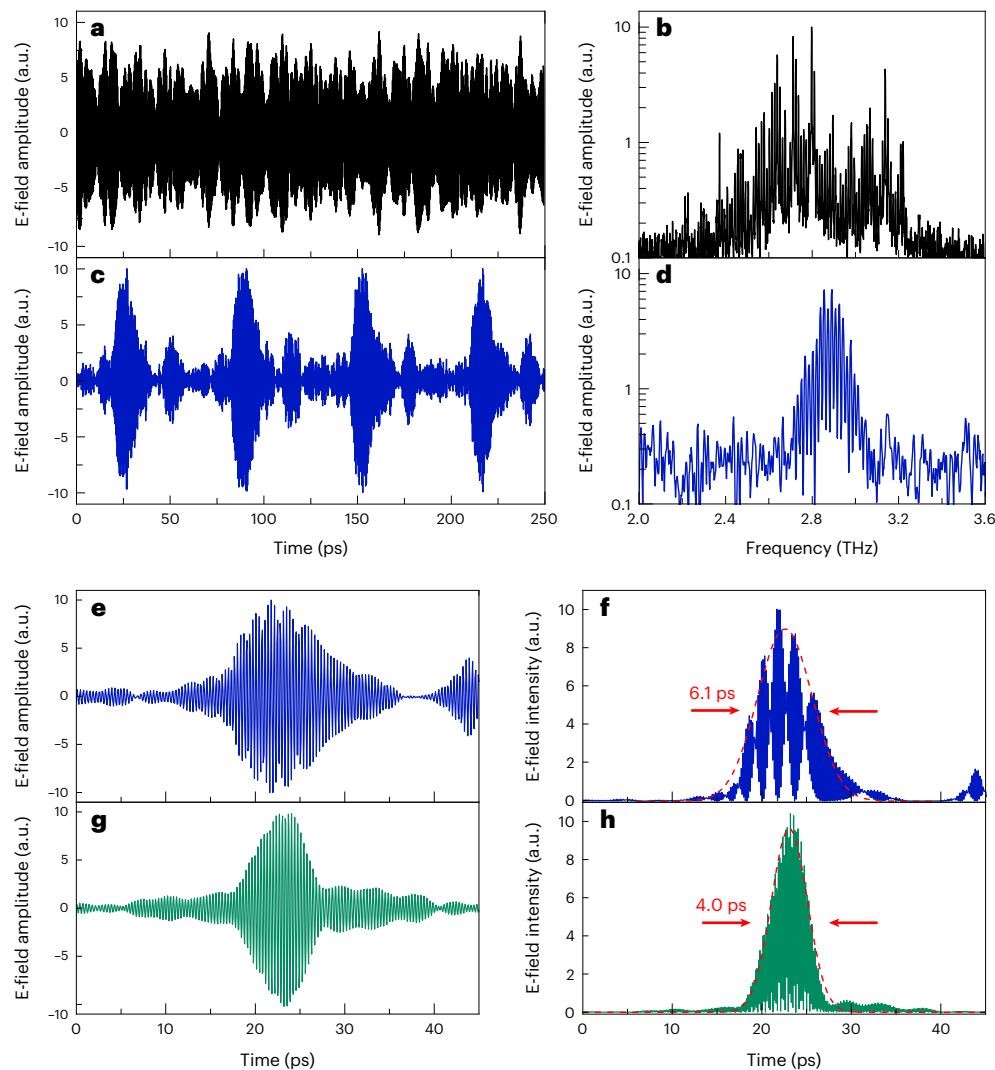


Fig. 3 | Terahertz TDS emission profiles. **a, b**, Time-domain emission profile of the reference QCL (without GSA; ref. 37) biased at 663 mA (**a**), and the corresponding Fourier frequency transform (**b**). **c, d**, Time-domain emission profile of the DGSA-QCL biased at 327 mA (**c**), and the corresponding Fourier frequency transform (**d**). **e, f**, Electric field amplitude profile of a pulse emitted by

the DGSA-QCL biased at 327 mA (**e**), and the corresponding intensity profile (**f**). The red dashed line is a Gaussian fit of the pulse with full-width at half-maximum (FWHM) of 6.1 ps. **g, h**, Electric field amplitude profile of a pulse emitted by the DGSA-QCL at 570 mA (**g**), and the corresponding intensity profile (**h**). The red dashed line is a Gaussian fit of the pulse with FWHM of 4.0 ps.

physical mechanism at the origin of the observed phenomenon. The active region dynamics are modelled employing a Lindblad-type approach^{51,52} and the quantum system represents a QCL period with periodic boundary conditions^{51,52} (Methods). The waveguide parameters used for the simulations are presented in Table 1. The simulated optical power of the last five roundtrip times (T_{rt}) outcoupled at the back facet in stationary operation, and the associated power spectrum, are shown in Fig. 4a,b. As in the experiment, at ~ 2.5 -times the threshold current a regular train of pulses is observed with a narrow beatnote (far below the numerical resolution limit) and a temporal pulse width (FWHM) of ~ 4.4 ps, consistent with the measured duration (4 ps). The resulting comb shows clear, narrow (far below the numerical resolution limit) and equidistant lines, with thirteen of them in a 10 dB power range. The slight asymmetry of the pulse is reproduced (compare Fig. 3h), and the optical power per comb tooth (0.15 mW for the highest, and 0.07 mW average for the teeth in a 10 dB power range) fits well to the measured ~ 0.12 mW. For comparison, enhancing the gain by increasing the doping density by $\sim 2.5\%$ reproduces the experimental breakdown of pulses at currents $350 \text{ mA} < I < 570 \text{ mA}$, that is, above the breakdown of the initial

Table 1 | Simulation parameters

Parameter	Value
Loss coefficient a_0	10.5 cm^{-1}
Saturable loss coefficient a_1	10.5 cm^{-1}
Saturation power P_s	42.5 mW
Saturable absorber recovery time τ_r	2.5 ps
Overlap factor	0.97
Centre frequency	3.0 THz
Mirror reflectivity (power)	70.88%
Refractive index	3.6
GVD factor β_2	$1.0 \times 10^{-22} \text{ s}^2 \text{ m}^{-1}$

comb state and before entering in the second stable comb regime (Fig. 4c,d), with the resulting chaotic behaviour. The simulated radiofrequency beatnote width ~ 400 MHz agrees very well with the experimental results in Fig. 2e.

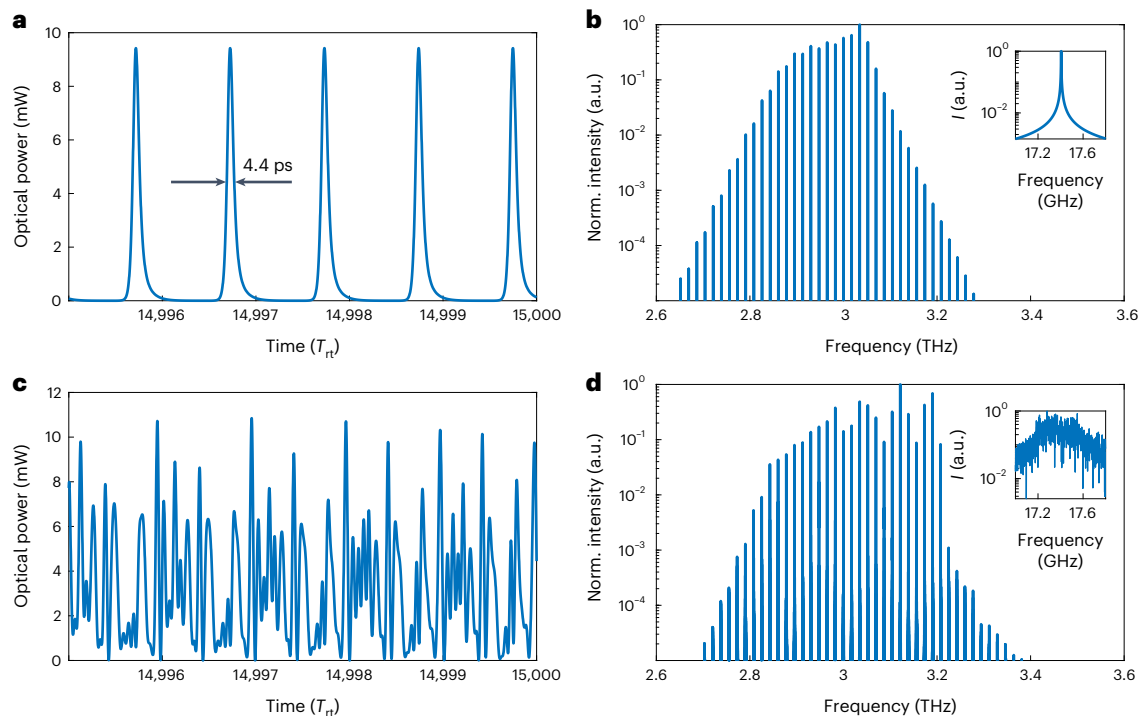


Fig. 4 | Maxwell–Bloch dynamical simulations. **a**, Instantaneous pulse power outcoupled at the right end facet in steady state operation at ~ 2.5 times the threshold current for $P_s = 42.5$ mW and $\tau_r = 2.5$ ps. **b**, Associated power spectrum computed from 15,000 roundtrips in steady state operation. Inset,

radiofrequency beatnote. The linewidth is substantially below the numerical frequency resolution (1.17 MHz). **c**, Outcoupled power with increased gain showing chaotic behaviour. **d**, Associated power spectrum. Inset, radiofrequency beatnote, showing a width of ~ 400 MHz.

To prove quantitatively the presence of mode-locking in the simulated optical field, we employ power and phase noise quantifiers M_{σ_P} and $M_{\Delta\Phi}$ (ref. 53), as:

$$M_{\sigma_P} = \frac{1}{N_{10}} \sum_{q=1}^{N_{10}} \sigma_{P_q}, \quad M_{\Delta\Phi} = \frac{1}{N_{10}} \sum_{q=1}^{N_{10}} \sigma_{\Delta\Phi_q},$$

respectively, with

$$\sigma_{P_q} = \sqrt{\langle (P_q(t) - \langle P_q(t) \rangle)^2 \rangle}, \quad \sigma_{\Delta\Phi_q} = \sqrt{\langle (\Delta\Phi_q(t) - \langle \Delta\Phi_q(t) \rangle)^2 \rangle}$$

where $P_q(t)$ represents the modal amplitudes and $\Delta\Phi_q(t)$ represents the modal phase differences between one mode and the adjacent, at time t for each mode $q = 1, \dots, N_{10}$, with N_{10} being the number of modes in the -10 dB spectral bandwidth.

In this framework, an optical frequency comb is present for $M_{\sigma_P} < 10^{-2}$ mW and $M_{\Delta\Phi} < 2 \times 10^{-2}$ rad. Regarding the pulsed mode of Fig. 4a,b, values of $M_{\sigma_P} = 3 \times 10^{-8}$ mW and $M_{\Delta\Phi} = 3 \times 10^{-5}$ rad are obtained. We can thus confirm an ultrastable mode-locked operation in this current range. Calculating the same parameters for the results of Fig. 4c,d, yields $M_{\sigma_P} = 0.13$ mW and $M_{\Delta\Phi} = 4.91$ rad. This increase proves the absence of mode-locking for higher gain, in agreement with our theory of pulse formation, as discussed below.

Discussion

One key observation to understand pulse formation in our DGSA-QCL is that the graphene stripes provide fast saturable absorption across the resonator length, while the gain also has a recovery time that is much faster (around 3 picoseconds for the present structure) than the roundtrip time²⁵. Ref. 54 suggests that mode-locked operation only occurs if the pulses are stabilized by a net gain window, whereas the standard passive mode-locking theory⁵⁴ does not provide

self-starting mode-locked pulse solutions for instantaneous gain and saturable absorption. These assumptions are relaxed in our experiments by the fact that both the gain and saturable absorber have a finite recovery time of a few picoseconds^{55,56}. As also pointed out in ref. 54, the constraints for self-starting passive mode-locking are further relaxed if a second, longer gain recovery time is present, as is typically the case for bound-to-continuum QCLs due to the electron transport across the miniband⁵⁷. But most importantly, deviations from the analytical theory of ref. 54 arise due to the unique design of our structure with a saturable absorber distributed along the entire Fabry–Perot cavity, which gives rise to effects such as cross-saturation and spatial hole burning. Furthermore, quantum coherence and nonlinear effects of the quantum active region have to be taken into account, requiring our detailed Maxwell–Bloch-type simulations presented in the Methods. The emergence of mode-locked pulses that are in close qualitative agreement with the measured ones confirms the validity of our model. Furthermore, this theoretical model allows us to clearly identify the saturable absorber as the element enabling mode-locked operation: decreasing the saturable absorber recovery time yields shorter pulses while considerably extending the recovery time results in a breakdown of mode-locking.

The numerical pulse duration of 4.4 ps is relatively close to the Fourier limit (3.1 ps). This suggests that the main limitation in terms of achievable pulse duration is the laser bandwidth and the chromatic dispersion. Furthermore, as mentioned above, the simulations indicate that an even faster saturable absorber recovery time would enable considerably shorter pulses; thus, further optimization of the waveguide structure, adjustments to the graphene optical properties and the employment of ultrabroadband (an octave) active regions could be adopted to enhance the emission bandwidth uniformity, effectively indicating a practical path to achieve sub-picosecond terahertz pulse generation.

Conclusion

We have shown 4.0 ps pulse generation from a passively mode-locked semiconductor terahertz laser using a unique graphene-based saturable absorber that is distributed along the entirety of the terahertz QCL cavity. This has overcome a long-standing bottleneck of realizing passive pulse generation from laser systems with ultrafast dynamics, where the gain recovery time is much shorter than the photon round trip time, and could be applied to other types of laser systems beyond terahertz QCLs. Exploiting the wide spectral gain of terahertz QCLs and the lithographic capability to embed miniaturized, highly nonlinear, intracavity graphene absorbers to produce short pulses without any external source or seeding system, could allow QCLs to become an attractive alternative to present-day terahertz TDS systems in spectroscopic and metrological applications. Although this work can naturally impact frequency comb spectroscopy, further improvements could impact other domains such as the dynamics of systems that need to be pumped at targeted terahertz frequencies. This will require shorter (sub-picosecond) and higher intensity pulses separated by longer round trip times, which could be achieved through longer or external cavities to increase the round-trip time, combined with pulse compression techniques (on-chip or external) to compensate for dispersion^{20,58}. It should also be noted that most femtosecond commercial systems in the visible/infrared rely on passive pulse generation, as this approach permits the shortest pulses and highest powers. Our work will hence open interesting application perspectives in spectroscopy, as there is currently no passive mode-locked system for the terahertz range.

Online content

Any methods, additional references, Nature Portfolio reporting summaries, source data, extended data, supplementary information, acknowledgements, peer review information; details of author contributions and competing interests; and statements of data and code availability are available at <https://doi.org/10.1038/s41566-023-01195-z>.

References

- Haus, H. A. Mode-locking of lasers. *IEEE J. Sel. Top. Quantum Electron.* **6**, 1173–1185 (2000).
- Perego, A. M. et al. Coherent master equation for laser modelocking. *Nat. Commun.* **11**, 311 (2020).
- Cundiff, S. T. & Ye, J. Phase stabilization of mode-locked lasers. *J. Mod. Opt.* **52**, 201–219 (2005).
- Du, T. et al. 1.2-W Average-power, 700-W peak-power, 100-ps dissipative soliton resonance in a compact Er:Yb co-doped double-clad fiber laser. *Opt. Lett.* **42**, 462–465 (2017).
- Tang, W. et al. High-peak-power mode-locking pulse generation in a dual-loss-modulated laser with BP-SA and EOM. *Opt. Lett.* **42**, 4820–4823 (2017).
- Rausch, S. et al. Controlled waveforms on the single-cycle scale from a femtosecond oscillator. *Opt. Express* **16**, 9739–9745 (2008).
- Zewail, A. H. Femtochemistry: atomic-scale dynamics of the chemical bond. *J. Phys. Chem. A* **104**, 5660–5694 (2000).
- Hänsch, T. W. Nobel Lecture: Passion for precision. *Rev. Mod. Phys.* **78**, 1297–1309 (2006).
- Fortier, T. & Baumann, E. 20 years of developments in optical frequency comb technology and applications. *Commun. Phys.* **2**, 1–16 (2019).
- Keller, U. et al. Semiconductor saturable absorber mirrors (SESAMs) for femtosecond to nanosecond pulse generation in solid-state lasers. *IEEE J. Sel. Top. Quantum Electron.* **2**, 435–453 (1996).
- Komarov, A., Leblond, H. & Sanchez, F. Passive harmonic mode-locking in a fiber laser with nonlinear polarization rotation. *Opt. Commun.* **267**, 162–169 (2006).
- Haus, H. A., Fujimoto, J. G. & Ippen, E. P. Structures for additive pulse mode locking. *JOSA B* **8**, 2068–2076 (1991).
- Lu, H., Xu, H., Zhao, J. & Hou, D. A deep ultraviolet mode-locked laser based on a neural network. *Sci Rep.* **10**, 116 (2020).
- Qin, Z. et al. Black phosphorus Q-switched and mode-locked mid-infrared Er:ZBLAN fiber laser at 3.5 μm wavelength. *Opt. Express* **26**, 8224–8231 (2018).
- Fülöp, J. A., Tzortzakidis, S. & Kampfrath, T. Laser-driven strong-field terahertz sources. *Adv. Opt. Mater.* **8**, 1900681 (2020).
- Gollner, C. et al. Highly efficient THz generation by optical rectification of mid-IR pulses in DAST. *APL Photon.* **6**, 046105 (2021).
- Vinokurov, N. Free electron lasers as a high-power terahertz sources. *J. Infrared Millim. Terahertz Waves* **32**, 1123–1143 (2011).
- Vitiello, M. S. & Tredicucci, A. Physics and technology of Terahertz quantum cascade lasers. *Adv. Phys. X* **6**, 1893809 (2021).
- Khalatpour, A. et al. Terahertz semiconductor laser source at –12 C. Preprint at <https://doi.org/10.48550/arXiv.2211.08125> (2022).
- Wang, F. et al. Short terahertz pulse generation from a dispersion compensated modelocked semiconductor laser. *Laser Photon. Rev.* **11**, 1700013 (2017).
- Barbieri, S. et al. Coherent sampling of active mode-locked terahertz quantum cascade lasers and frequency synthesis. *Nat. Photon.* **5**, 377–377 (2011).
- Bachmann, D. et al. Short pulse generation and mode control of broadband terahertz quantum cascade lasers. *Optica* **3**, 1087 (2016).
- Wang, F. et al. Ultrafast response of harmonic modelocked THz lasers. *Light: Sci. Appl.* **9**, 51 (2020).
- Piccardo, M. & Capasso, F. Laser frequency combs with fast gain recovery: physics and applications. *Laser Photon. Rev.* **16**, 2100403 (2022).
- Riepl, J. et al. Field-resolved high-order sub-cycle nonlinearities in a terahertz semiconductor laser. *Light: Sci. Appl.* **10**, 246 (2021).
- Derntl, C. G. et al. Gain dynamics in a heterogeneous terahertz quantum cascade laser. *Appl. Phys. Lett.* **113**, 181102 (2018).
- Tzenov, P. et al. Passive and hybrid mode locking in multi-section terahertz quantum cascade lasers. *New J. Phys.* **20**, 053055 (2018).
- Henry, N., Burghoff, D., Hu, Q. & Khurgin, J. B. Study of spatio-temporal character of frequency combs generated by quantum cascade lasers. *IEEE J. Sel. Top. Quantum Electron.* **25**, 1–9 (2019).
- Wang, C. Y. et al. Mode-locked pulses from mid-infrared quantum cascade lasers. *Opt. Express* **17**, 12929–12943 (2009).
- Kuizenga, D. & Siegman, A. FM and AM mode locking of the homogeneous laser—part I: theory. *IEEE J. Quantum Electron.* **6**, 694–708 (1970).
- Prati, F. et al. Soliton dynamics of ring quantum cascade lasers with injected signal. *Nanophotonics* **10**, 195–207 (2021).
- Meng, B. et al. Dissipative Kerr solitons in semiconductor ring lasers. *Nat. Photon.* **16**, 142–147 (2022).
- Neu, J. & Schmuttenmaer, C. A. Tutorial: an introduction to terahertz time domain spectroscopy (THz-TDS). *J. Appl. Phys.* **124**, 231101 (2018).
- Talukder, M. A. & Menyuk, C. R. Self-induced transparency modelocking of quantum cascade lasers in the presence of saturable nonlinearity and group velocity dispersion. *Opt. Express* **18**, 5639 (2010).
- Choi, H. et al. Ultrafast Rabi flopping and coherent pulse propagation in a quantum cascade laser. *Nat. Photon.* **4**, 706–710 (2010).
- Li, L. et al. Broadband heterogeneous terahertz frequency quantum cascade laser. *Electron. Lett.* **54**, 1229–1231 (2018).
- Garrasi, K. et al. High dynamic range, heterogeneous, terahertz quantum cascade lasers featuring thermally tunable frequency comb operation over a broad current range. *ACS Photon.* **6**, 73–78 (2019).

38. Bianchi, V. et al. Terahertz saturable absorbers from liquid phase exfoliation of graphite. *Nat. Commun.* **8**, 15763 (2017).
 39. Brida, D. et al. Ultrafast collinear scattering and carrier multiplication in graphene. *Nat. Commun.* **4**, 1987 (2013).
 40. Tomadin, A., Brida, D., Cerullo, G., Ferrari, A. C. & Polini, M. Nonequilibrium dynamics of photoexcited electrons in graphene: collinear scattering, Auger processes, and the impact of screening. *Phys. Rev. B* **88**, 035430 (2013).
 41. Paiella, R. et al. Self-mode-locking of quantum cascade lasers with giant ultrafast optical nonlinearities. *Science* **290**, 1739–1742 (2000).
 42. Hafez, H. A. et al. Terahertz nonlinear optics of graphene: from saturable absorption to high-harmonics generation. *Adv. Opt. Mater.* **8**, 1900771 (2020).
 43. Consolino, L. et al. Fully phase-stabilized quantum cascade laser frequency comb. *Nat. Commun.* **10**, 1–7 (2019).
 44. Mezzapesa, F. P. et al. Terahertz frequency combs exploiting an on-chip, solution-processed, graphene-quantum cascade laser coupled-cavity. *ACS Photon.* **7**, 3489–3498 (2020).
 45. Burghoff, D., Yang, Y., Reno, J. L. & Hu, Q. Dispersion dynamics of quantum cascade lasers. *Optica* **3**, 1362 (2016).
 46. Oustinov, D. et al. Phase seeding of a terahertz quantum cascade laser. *Nat. Commun.* **1**, 69 (2010).
 47. Beiser, M., Opačak, N., Hillbrand, J., Strasser, G. & Schwarz, B. Engineering the spectral bandwidth of quantum cascade laser frequency combs. *Opt. Lett.* **46**, 3416–3419 (2021).
 48. Opačak, N., Cin, S. D., Hillbrand, J. & Schwarz, B. Frequency comb generation by Bloch gain induced giant Kerr nonlinearity. *Phys. Rev. Lett.* **127**, 093902 (2021).
 49. Cavalié, P. et al. High order sideband generation in terahertz quantum cascade lasers. *Appl. Phys. Lett.* **102**, 221101 (2013).
 50. Gallot, G., Zhang, J., McGowan, R. W., Jeon, T.-I. & Grischkowsky, D. Measurements of the THz absorption and dispersion of ZnTe and their relevance to the electro-optic detection of THz radiation. *Appl. Phys. Lett.* **74**, 3450–3452 (1999).
 51. Tzenov, P., Burghoff, D., Hu, Q. & Jirauschek, C. Time domain modeling of terahertz quantum cascade lasers for frequency comb generation. *Opt. Express* **24**, 23232–23247 (2016).
 52. Jirauschek, C., Riesch, M. & Tzenov, P. Optoelectronic device simulations based on macroscopic Maxwell–Bloch equations. *Adv. Theory Simul.* **2**, 1900018 (2019).
 53. Silvestri, C., Columbo, L. L., Brambilla, M. & Gioannini, M. Coherent multi-mode dynamics in a quantum cascade laser: amplitude- and frequency-modulated optical frequency combs. *Opt. Express* **28**, 23846–23861 (2020).
 54. Haus, H. A. Theory of mode locking with a fast saturable absorber. *J. Appl. Phys.* **46**, 3049–3058 (1975).
 55. Pogna, E. A. A. et al. Hot-carrier cooling in high-quality graphene is intrinsically limited by optical phonons. *ACS Nano* **15**, 11285–11295 (2021).
 56. Sun, Z. et al. Graphene mode-locked ultrafast laser. *ACS Nano* **4**, 803–810 (2010).
 57. Choi, H. et al. Gain recovery dynamics and photon-driven transport in quantum cascade lasers. *Phys. Rev. Lett.* **100**, 167401 (2008).
 58. Mezzapesa, F. P. et al. Tunable and compact dispersion compensation of broadband THz quantum cascade laser frequency combs. *Opt. Express* **27**, 20231–20240 (2019).
- Publisher's note** Springer Nature remains neutral with regard to jurisdictional claims in published maps and institutional affiliations.
- Springer Nature or its licensor (e.g. a society or other partner) holds exclusive rights to this article under a publishing agreement with the author(s) or other rightsholder(s); author self-archiving of the accepted manuscript version of this article is solely governed by the terms of such publishing agreement and applicable law.
- © The Author(s), under exclusive licence to Springer Nature Limited 2023

Methods

Fabrication and graphene preparation

Fabry–Perot laser bars are fabricated in a metal–metal waveguide configuration via Au–Au thermocompression wafer bonding of a 17- μm -thick active region onto a highly doped GaAs substrate. This is followed by the removal—through a combination of mechanical lapping and wet etching—of the host GaAs substrate of a material grown by molecular beam epitaxy. An $\text{Al}_{0.5}\text{Ga}_{0.5}\text{As}$ etch stop layer is then removed using HF etching. Vertical sidewalls are defined by inductively coupled plasma etching of the laser bars to provide uniform current injection. A Cr/Au (10 nm/150 nm) top contact is then deposited along the centre of the ridge surface, leaving a thin region uncovered along the ridge edges and two stripes uncovered 12 μm from the centre of the cavity; 3 μm -wide nickel (5-nm-thick) side absorbers were then deposited over the lateral uncovered region using a combination of optical lithography and thermal evaporation. These lossy side absorbers are intended to inhibit lasing of the higher order lateral modes by increasing their threshold gain⁴⁹.

The multilayer graphene sample is prepared and transferred on the stripes, using a wet transfer technique: A4-950K ply (methyl-methacrylate) polymer (PMMA) is spin coated at 2,000 r.p.m. on the surface of a single-layer graphene (SLG) sample (1 cm \times 1 cm) grown on copper via chemical-vapour-deposition. After 1 min on a hot plate at 90 °C, the sample is placed in a solution of 1 g of ammonium persulfate and 40 ml of deionized water to etch the copper substrate. Once the copper etching is complete, the PMMA-SLG film is transferred in a beaker with deionized water and then lifted with a second copper-graphene square to obtain a bilayer graphene sample. This sample is left to dry overnight and finally the PMMA is removed with acetone. The copper of the bilayer graphene is etched with the same technique, and then lifted by another SLG on copper. This process is repeated until the desired MLG thickness is reached, in our case seven layers. The MLG is transferred onto the QCL top contact and then removed from the sides of the laser cavity and from the top gold contact by oxygen reactive ion etching.

The backside of the substrate is then lapped down to 150 μm for thermal management and enable continuous-wave operation. Laser bars (50 μm wide and 2.2 mm long) are then cleaved and the device mounted on a copper bar, wire bonded, and then mounted onto the cold finger of a helium continuous-flow cryostat. The fabrication flow-chart is presented in Supplementary Fig. 1.

Model

The active region dynamics is modelled based on a Lindblad-type approach, where the quantum system represents a QCL period with periodic boundary conditions^{51,52}. We performed self-consistent carrier transport simulations of the active region to extract the corresponding eigenenergies, optical dipole moments as well as the scattering and dephasing rates⁵¹. For simplicity, the dynamical model only takes into account the 2.5 THz design, yielding agreement with experiments. The model system comprises nine quantized energy states, including two upper- and one lower-laser levels. In the common rotating wave/slowly varying amplitude approximation, the optical cavity field is described by complex amplitudes $E^\pm(z,t)$ for the forward and backward travelling electric field component, and the propagation given by⁵²

$$v_g^{-1}\partial_t E^\pm \pm \partial_z E^\pm = p^\pm - \alpha(P)E^\pm - i\frac{\beta_2}{2}\partial_z^2 E^\pm \quad (1)$$

Here, z and t are the propagation coordinate and time, respectively; v_g denotes the group velocity; $p^\pm(z,t)$ is computed from the Lindblad equation^{51,52} and contains the polarization due to the quantized states of the QCL active region; and β_2 describes the background GVD. The total power loss coefficient is $a = a_0 + a_s$, where the saturable absorber is modelled by the saturable contribution $a_s(z,t)$ using⁵⁹:

$$\partial_t a_s = -\frac{P}{\tau_r P_s} a_s - \frac{a_s - a_1}{\tau_r} \quad (2)$$

with the optical power $P \propto |E^+|^2 + |E^-|^2$ and saturable absorber recovery time τ_r . Electromagnetic simulations yield $a_0 = a_1 = 10.5 \text{ cm}^{-1}$ (Fig. 1e). The saturation power P_s depends on the electric field strength and orientation in the graphene stripes, and hence it does not correspond to the saturation intensity of the MLG itself as it could be retrieved through z -scan measurements, or from considerations on the number of layers and doping level, but rather to the effective value for the transverse waveguide mode; it is therefore the only fitting parameter in our simulation. The resulting Maxwell–Bloch-type model is numerically solved over 26,000 roundtrips to ensure convergence to steady state⁵¹.

Data availability

The data presented in this study are available on reasonable request from the corresponding author.

Code availability

The relevant computer codes supporting this study are available from the authors on reasonable request.

References

59. Kurtner, F. X., der Au, J. A. & Keller, U. Mode-locking with slow and fast saturable absorbers—what's the difference? *IEEE J. Sel. Top. Quantum Electron.* **4**, 159–168 (1998).

Acknowledgements

This work was supported by the European Research Council through the ERC Consolidator Grant (681379) SPRINT (MSV), FET Open project EXTREME IR (944735) (MSV, SSD), Quanterra Project QATACOMB (MSV, SSD, CJ), ERC GSYNCOR (ACF), HETERO2D (ACF), EIC CHARM (ACF), the French National Research Agency (ANR-18-CE24-0013-02 - 'TERASEL') (SD), and the EPSRC (UK) programme grant 'HyperTerahertz' (EP/PO21859/1) (EHL, LL, AGD), EP/LO16087/1, EP/KO1711X/1, EP/KO17144/1, EP/NO10345/1, EP/V000055/1 (ACF) and Graphene Flagship (MSV, ACF).

Author contributions

M.S.V. and V.P. conceived the concept. E.R. fabricated the devices, set up the transport and optical experiments. V.P. performed numerical simulations and interpreted the data. E.R., S.S.D., S.K. and A.D.V. acquired the experimental data. L.L., A.G.D. and E.H.L. grew by the QCL structure molecular beam epitaxy. C.J. and L.S. developed the theoretical model. The manuscript was written by M.S.V. and V.P. M.S.V. coordinated and supervised the project. All authors contributed to the final version of the manuscript and discussed the results.

Competing interests

The authors declare no competing interests.

Additional information

Supplementary information The online version contains supplementary material available at <https://doi.org/10.1038/s41566-023-01195-z>.

Correspondence and requests for materials should be addressed to Miriam S. Vitiello.

Peer review information *Nature Photonics* thanks Mahmood Bagheri and the other, anonymous, reviewer(s) for their contribution to the peer review of this work.

Reprints and permissions information is available at www.nature.com/reprints.